ORIGINAL ARTICLE

Turbulence and equatorial waves in moist and dry shallow-water flow, excited through mesoscale stochastic forcing

J. Schröttle[1] | D.L. Suhas[2,4] | N. Harnik[1] | J. Sukhatme[2,3]

[1]Department of Geophysics, School of Earth Sciences, Tel Aviv University, Israel.

[2]Centre for Atmospheric and Oceanic Sciences, Indian Institute of Science, Bangalore, 560012, India.

[3]Divecha Centre for Climate Change, Indian Institute of Science, Bangalore, 560012, India.

[4]Department of Earth and Planetary Science, University of California, Berkeley, USA

Correspondence
J. Schröttle, Department of Geophysics, Tel Aviv University, Israel
Email: josefs@mail.tau.ac.il

Funding information
This work was conducted in a joint research project between the Israeli Science Foundation (grant number 2713/17) and University Grants Commission, India (grant number F6-3/2018).

Turbulence and large-scale waves in the tropical region are studied using the spherical shallow-water equations. With mesoscale vorticity forcing, both moist and dry systems show an upscale transfer of kinetic energy that is dominated by rotational modes, scales as a power-law with $-5/3$ exponent, requires eddy-eddy interactions and ranges from the forcing scale to the respective equatorial deformation radius. At larger planetary scales, the divergent component of the energy increases and we see a footprint of tropical waves. The dry system shows a signature of the entire family of equatorial waves, while the moist simulations only show low frequency Rossby, Kelvin and mixed Rossby gravity waves with an equivalent depth that matches rapid condensation estimates. Initially, runs with interactive moisture exhibit a weak inverse transfer of moisture variance as well exponential growth across a range of length scales. This results in an equilibrium moist energy spectrum obeying a -2 power-law and the formation of moisture aggregates. Once formed, aggregates propagate westward in the tropics with speeds of the order of a few meters per second. In contrast, forcing divergence does not excite an inverse transfer, and injected energy remains trapped at the forcing scale. Height (i.e., temperature or mass) forcing results in a peak at the forcing scale, but also generates large-scale waves and projects on to rotational modes that undergo an inverse energy transfer. Similarly, forcing the moisture field by itself produces an inverse transfer of rotational energy and a well formed large-scale equatorial wave spectrum. Notably, both the height- and moisture-forced inverse transfers are different in nature. Specifically, they require the presence of ambient planetary rotation. In all, these experiments demonstrate that the vortical and divergent wind are inextricably linked with the evolving moisture field, and that large-scale equatorial waves co-exist with synoptic-scale moist turbulence.

KEYWORDS

Moist Turbulence, Moist Shallow Water Equations, Equatorial Waves, Aggregation, Equatorial Jets

1 | INTRODUCTION

Waves in the tropical atmosphere appear as coherent cloud patters and have been measured by geostationary satellites at temporal resolutions ranging from days to intraseasonal time scales (e.g., Takayabu, 1994; Wheeler and Kiladis, 1999). Specifically, waves have been identified in wavenumber-frequency analyses of outgoing longwave radiation (OLR) that is often used as a proxy for deep convection, and even in other variables such as zonal winds from reanalysis data (Hendon and Wheeler, 2008). Satellite data also allows for the detection of slowly propagating bands of water vapor in a relatively dry atmospheric column (Schröttle et al., 2020). Some of the identified tropical waves correspond to classical dry modes in solutions of shallow-water systems in the equatorial region (Matsuno, 1966) — albeit, with a smaller equivalent depth (Kiladis et al., 2009). While a theoretical estimate of the reduced equivalent depth, especially outside the so-called rapid condensation limit, is a challenge, lower wave speeds are attributed to the dynamical coupling with water vapor (Gill, 1982). Indeed, the importance of moisture, and its advection, for convectively coupled equatorial waves (CCEWs; Wheeler et al., 2000) has been highlighted in controlled cloud resolving simulations (Kuang, 2008b). The generation of such slow CCEWs has been noted in complex and simplified general circulation models (GCMs; Lin et al., 2006; Frierson, 2007). Of course, mismatches between observations and fully complex models in terms of wave speeds and wave structure are the subject of ongoing scrutiny (Lin et al., 2008). There is also an extensive body of literature on simplified models, i.e., those with one or two vertical modes and prescribed heating, that explore linear instabilities to account for the generation of CCEWs (see, for example, Mapes, 2000; Majda and Shefter, 2001). Such linearized models with simplified vertical structure but explicit moisture evolution have also been examined in the context of equatorial waves (Kuang, 2008a; Khouider and Majda, 2008). Interestingly, equatorial Rossby waves are not included in these efforts and are usually dealt with separately (Chatterjee and Goswami, 2004). Though, both tropical Rossby and Kelvin waves with suitably reduced speeds have been observed in initial value problems with a nonlinear moist shallow-water system (Suhas and Sukhatme, 2020). It is important to note that these waves exist at large spatial scales, indeed, most wavenumber-frequency diagrams display variability from approximately wavenumber 1 to 10, or from four to five thousand kms to the planetary scale (Wheeler and Kiladis, 1999; Wheeler et al., 2000; Hendon and Wheeler, 2008).

At relatively smaller scales, from about 50 to 2000 km, i.e., the mesoscales through to synoptic scales, the midlatitude atmospheric kinetic energy (KE) is observed to follow power-law scaling (Nastrom and Gage, 1985). Specifically, in the midlatitude upper troposphere KE follows $-5/3$ and -3 exponents in the range of 50–500 km (mesoscales) and above (up to about 2000 km; synoptic scales), respectively (Nastrom and Gage, 1985). The steeper -3 exponent is generally accepted to be a result of a forward enstrophy transfer quasi-geostrophic regime (Charney, 1971; Boer and Shepherd, 1983; Bartello, 1995). The mesoscale range is associated with a forward energy transfer (Cho and Lindborg, 2001; Lindborg and Cho, 2001), though there are different candidates — ranging from rotating stratified turbulence with wave mode dominance (Kitamura and Masuda, 2006; Sukhatme and Smith, 2008; Vallgren et al., 2011), purely stratified dynamics (Lindborg, 2007; Lindborg and Brethouwer, 2007), balanced surface quasi-geostrophic turbulence (Tulloch and Smith, 2006) to inertia-gravity waves (Callies et al., 2014) — proposed for the $-5/3$ scaling. The correct choice from among these possibilities depends on the ratio of energy in rotational and divergent components of the horizontal mesoscale flow field (Callies et al., 2014; Lindborg, 2015), which itself appears to be non-universal (Bierdel et al., 2016).

In the tropics, below the planetary-scale equatorial waves, there lies the mesoscale moist convective range. Here, the situation regarding the mesoscale spectrum is likely more complicated due to the effects of moisture on turbulence. In fact, in a f−plane study, Waite and Snyder (2013) noted that injection of energy due to latent heating enhanced the role of divergent components in moist baroclinic waves. On the other hand, numerical simulations of tropical cyclones showed a forward energy transfer and $-5/3$ KE power-law dominated by rotational modes, at scales below 500 km in the upper troposphere (Wang et al., 2018). But, *in situ* aircraft data taken from flights through hurricanes paint a more diverse picture with mesoscale slopes going from $-5/3$ to -3 depending on the strength of systems (Vonich and Hakim, 2018). More broadly, simulations using the Weather Research and Forecast (WRF) model, initialized with temperature anomalies in a moist environment show that buoyancy via moist convection plays an important role in the mesoscale spectrum in the tropical region (Sun et al., 2017). In these simulations, rotational and divergent modes were observed to have an almost equal contribution to the total horizontal KE of the flow, both of which scaled with a $-5/3$ exponent. But, clear cascades could not be identified and buoyancy was noted to inject energy at all scales. Interestingly, two-dimensional moist stratified turbulence also showed the establishment of $-5/3$ scaling from an initially flat spectrum via (unequal) energy growth at all scales (Sukhatme et al., 2012). Further, upscale energy cascades from deep convective events up to the mesoscale have been noted in large-eddy simulations of the tropical region (Vallis et al., 1997).

Given this situation, we study tropical turbulence (both moist and dry) using a shallow-water system with an eye towards the mesoscales, synoptic and planetary scales. In essence, rather than isolating any one of these ranges, given their interactions, we hope to simulate them simultaneously. The shallow-water system affords us the possibility of resolving this extended range of scales efficiently and is also possibly the simplest model to include the relevant dynamical ingredients required to make a connection to the tropical atmosphere (Zeitlin, 2018). In a turbulent context, explorations of the decaying and forced-dissipative spherical shallow-water systems have been without moisture and have almost exclusively focused on extratropical phenomena such as the emergence of jets and vortices (see, for example, Scott and Polvani, 2007). Though, in recent years, moist shallow-water systems have been quite widely used in a tropical context. For example, studies aimed at the Madden-Julian Oscillation and other intraseasonal modes have used the shallow-water framework with condensation, evaporation and either explicit (Rostami and Zeitlin, 2019a,b; Vallis and Penn, 2020), or implicit (Solodoch et al., 2011; Yang and Ingersoll, 2013) treatment of water vapor. In addition, the roles of moisture gradients (Sobel et al., 2001; Sukhatme, 2013; Monteiro and Sukhatme, 2016; Suhas and Sukhatme, 2020) and convergence in the boundary layer (Wang et al., 2016) have also been studied. All of these studies focus on the generation of large-scale waves and do not consider turbulent solutions.

Here we use a moist shallow-water model and follow the evolution of vorticity, divergence, height and moisture - together with their respective variances (which constitute the different energy forms in the model). Our goal is to understand how energy transfers across scales from the mesoscale, where the forcing is applied, up to planetary scales. The specific questions we address include, (i) Can large-scale equatorial waves be excited with random mesoscale forcing through an upscale transfer of KE? (ii) What are the differences in the energy transfer and excited large-scale waves (if any) between dry and moist turbulence? (iii) How do rotational and divergent of KE differ in the turbulent solution when moisture enters the dynamics? (iv) Does moisture undergo an inverse transfer of energy leading to aggregation? (v) How does the energy transfer among different scales depend on the nature of the forcing employed? For example, given both of their physical relevance, how does vorticity forcing differ from divergence forcing? (vi) Do height and moisture forcing have significant impacts on the dynamics, i.e., are they able to excite an upscale energy transfer, or do they lead to the formation of large-scale equatorial waves? In all, the answers to these questions should help in developing an appreciation for the establishment of a hierarchy of structures from mesoscales to planetary scales, and the role of dynamically interactive moisture in the establishment of these tropical atmospheric features. Further, the scaling of spectra that emerge here could be of use in interpreting analogous results from more complicated models or observations of the tropical atmosphere.

2 | SHALLOW-WATER SIMULATION CONFIGURATION

We consider the moist shallow-water equations on a sphere with isotropic stochastic forcing for a single layer in the lower atmosphere on top of a moist saturated aqua planet. Following Gill (1982), the shallow-water equations with the presence of moisture have been formulated by Bouchut et al. (2009), and a detailed discussion of this system can be found in the textbook by Zeitlin (2018). In vorticity-divergence form these read,

$$\begin{aligned}
\partial_t \zeta &= -\nabla \cdot (\zeta \mathbf{v}) + f_\zeta - \zeta/\tau, \\
\partial_t \delta &= \nabla \times (\zeta \mathbf{v}) \cdot \hat{k} - \Delta \left(gh + \mathbf{v}^2/2 \right) + f_\delta - \delta/\tau, \\
\partial_t h &= -\nabla \cdot (h \mathbf{v}) - L\, q^+/\tau_c - L\, q^-/\tau_e + f_h - (h - H)/\tau, \\
\partial_t q &= -\nabla \cdot (q \mathbf{v}) + f_q - q^+/\tau_c - q^-/\tau_e,
\end{aligned} \tag{1}$$

where ζ is the absolute vorticity and δ is the divergence of the horizontal wind $\mathbf{v}$. In the divergence equation, $\nabla \times (\zeta \mathbf{v}) \cdot \hat{k}$ is the vertical component of the curl. The height of the layer is h and H is its global mean. Moisture q is composed of a background state (q_s) and a perturbation (q'). The geopotential is gh, where g is the gravitational constant of 9.81 m s^{-2}. Δ is the two-dimensional Laplacian. Linear drag in vorticity, divergence, and height equation mimic friction and radiative damping (Scott and Polvani, 2008). The associated time scale τ is 500 days. τ_c and τ_e are the time scales for condensation and evaporation, respectively. These time scales and moisture parameterization is further discussed in Section 2.1. To remove energy from the flow at small scales, we apply hyperdiffusion (of order 4) as in classic approaches to stochastically forced turbulent flows (McWilliams, 1984; Frisch and Sulem, 1984; Vallis and Maltrud, 1993). The equations are solved on a sphere by employing the efficient spectral transform library SHTNS (Schaeffer, 2013), on a grid consisting of 512×256 mesh points in longitude and latitude, while using an advection time step of $\Delta t = 50$ s. The forcing components act separately in vorticity, divergence, height and moisture equation and are denoted with: f_ζ, f_δ, f_h, and f_q, respectively. In the absence of forcing, drag and dissipation, the system conserves moist potential vorticity and moist enthalpy (Monteiro and Sukhatme, 2016). In fact, when the background saturation field is allowed to vary in space, the conservation of moist potential vorticity proves to be a useful guideline for the generation and propagation of moist Rossby waves (Suhas and Sukhatme, 2020).

2.1 | General properties of the shallow-water system and eddy energy

Moisture is allowed to fluctuate around the saturated state q_s, and while being advected by the flow it is subject to condensation and evaporation (Zeitlin, 2018). Condensation occurs immediately when the moist parcel is oversaturated: in regions of $q^+ := q - q_s$, where $q - q_s > 0$. When undersaturated: in regions of $q^- := q - q_s$, where $q - q_s < 0$, a parcel picks up moisture via evaporation. We assume that there is an infinite reservoir of moisture and the saturation field (q_s), which is fixed, can be isotropic and constant throughout the simulations (Bouchut et al., 2009; Rostami and Zeitlin, 2017, 2019a,b), or be a prescribed function of space (Monteiro and Sukhatme, 2016; Sobel et al., 2001; Sukhatme, 2013; Suhas and Sukhatme, 2020; Bembenek et al., 2021). Here, both condensation and evaporation follow Betts-Miller protocols (Rostami and Zeitlin, 2017), and these take place with timescales τ_c and τ_e, respectively. Observations suggest a time scale of $1 - 12$ h for τ_c (Frierson et al., 2004). We set the evaporation time scale for most of the presented experiments to $\tau_e = 1$ day and $\tau_c = 1/5$ day, taking into account that evaporation of cloud droplets takes more time than the formation of clouds through condensation in deep convection. Though, in some cases, we have also used $\tau_c = \tau_e$ and variations of these timescales from a few hours to a day do not affect the results. In fact, experiments by Suhas and Sukhatme (2020) with this numerical code have shown that results are independent of choosing the evaporation and condensation time scale, as long as both are smaller than one day. All simulations represent a lower layer in the atmosphere, so a sink term in the equation for its depth can also be thought of as a mass loss term due to convective updrafts (Bouchut et al., 2009), or a gain term may occur due to downdrafts.

Overall, simulations take about a few hundred days to reach a quasi-equilibrium state. Here, all simulations are run up to at least 1000 days to create appropriate fields for statistical post-processing. All experiments with a dry atmosphere are run with a global mean depth of 100 m, this keeps the shallow-water wave speed at least one order of magnitude below the speed of sound waves. To allow for moist Kelvin waves with typical phase speeds close to tropical values of approximately 20 m s^{-1}, we choose $Q = \max(q_s) = 50$ g kg^{-1} and $L \leq 1$ m / g kg^{-1}, with a resulting reduced shallow-water depth of 50 m for all moist experiments. Mean profiles and spectra are presented for single days (to show the development of turbulence), as well as averaged over several days within a time period of a few hundred days during quasi-stable equilibrium. For a more robust picture, we run 80 ensemble simulations with random isotropic forcing of the same magnitude. A detailed description of all experiments performed is presented in Table 1. To describe the evolving upscale energy cascade that is excited through the forcing of vorticity at the mesoscale, we begin to characterize the latitudinal evolution of eddy energies: regarding eddies as fluctuations from a zonal mean, we denote them as $(\cdot)'$ and a zonal mean by an overbar $\overline{(\cdot)}$. Eddy kinetic and potential energy are column integrated to retrieve units of J m^{-2} (Salmon, 1998). This gives, $KE = 0.5\,\rho\,H\,(u'u' + v'v')$, where $u'u'$ and $v'v'$ are zonal and meridional wind variance. Eddy PE is $0.5\,\rho\,g h'h'$, with ρ as a unit density of 1 kg m^{-3} and $h'h'$ as the height field variance. Similarly, we define an eddy moist energy as $0.5\,\rho\,g\,L^2\,q'q'$ in units J m^{-2} and proportional to moisture field variance $q'q'$. In the following, divergent and vortical modes of eddy KE are calculated, as both can be completely separated in wavenumber space, while their sum forms eddy KE (Appendix A). Thus, we refer to vortical/divergent modes of eddy KE to vortical/divergent eddy KE.

2.2 | Key features of the forcing fields in the moist and dry models

Stochastic forcing in numerical weather prediction traditionally represents unresolved physical processes and leads to a numerical solutions that cover a broader range of possible atmospheric flow scenarios (Palmer, 2001). The stochastic forcing employed is formulated as the Laplacian of a time-dependent stream function Ψ to represent vorticity forcing, or potential Φ to represent divergence forcing, that continuously forces the system in a wavenumber range $k_0 \pm 2$, where k_0 is the forcing scale. By construction, the direct forcing of vorticity leads to a flow free of divergence and vice versa. The only way to create divergence or vorticity that was not forced directly is by non-linear effects, or interaction with planetary vorticity f. In this work, we are interested in the formation of large scales from small-scale forcing, i.e., forcing is typically in the mesoscales at approximately 400 km, although these simulations have been repeated with forcing at smaller scales between 80-100 km (not shown). The forcing in each equation is applied separately and not in combination to study their individual flow response at synoptic and planetary scales. Further, we mainly force the vorticity and divergence fields individually as these represent physically meaningful ways of injecting kinetic energy into the system. Specifically, forcing via the vorticity equation is a means of representing the effect of smaller-scale unresolved dynamics on the column integrated shallow-water system (Scott and Polvani, 2008) and also reminds of mesoscale cyclones placed at random locations in the domain (Vallis et al., 1997). On the other hand, divergent forcing, which represents the influence of converging and diverging regions in convective events, is a way to mimic the small scale nature of the real-world divergent field (Koshyk and Hamilton, 2001). In addition to vorticity and divergence forcing, we also consider forcing f_h; indeed, recently, small-scale forcing of the height in a shallow-water setup has been used for investigating the background spectrum and waves in the tropics (Garfinkel et al., 2021). Height in shallow-water system can be interpreted as temperature of the fluid layer, and following Gill (1980), forcing via heat sources, both stationary and moving, steady and time dependent, have a long history in tropical dynamics. More broadly, one of the outstanding issues in the formation of large-scale moist tropical systems is the transfer of energy through the mesoscales (see, for example, Simpson et al., 1997, for a discussion in the context of tropical cyclones), and these mesoscales are composed of significant vorticity, divergence and moisture anomalies. Hence, in our final suite of experiments we consider the influence of forcing the moisture field by itself. The effects of forcing an "auxiliary" field such as moisture which dynamically couples with the governing equations has not received attention, and the view we adopt is that examining the influence of each of these forcing functions individually might help develop a better understanding of the scale interactions in the tropics, especially in the presence of moisture.

3 | DRY SIMULATIONS

We begin with the dry equations and isotropic vorticity forcing at small scales (wave number 100, i.e., approximately 400 km) over the entire sphere. The stationary tropical wavenumber-frequency spectrum from this simulation is shown in Figure 1a. Near the classical dispersion relations for Rossby, Yanai, Kelvin, and inertia gravity waves (Matsuno, 1966), the wavenumber-frequency diagram shows increased intensity at discrete points in space and time (Vallis, 2017; Suhas and Sukhatme, 2020; Garfinkel et al., 2021). Interestingly, the waves appear as clear maxima aligned with theoretical linear dispersion relations on top of a red background spectrum. Further, almost all the wave activity is concentrated at large scales, i.e., below wavenumber 20, or, above ≈3500 km. The signature of waves at such large scales is consistent with idealized, three-dimensional, triply periodic $f-$ plane numerical experiments (Asselin et al., 2018). We emphasize that no background has been removed in Figure 1a, indeed the high sampling rate allows the individual peaks to stand out over the background.

On an f-plane, vortical triad interactions of the shallow-water system form the quasi-geostrophic equations and support an

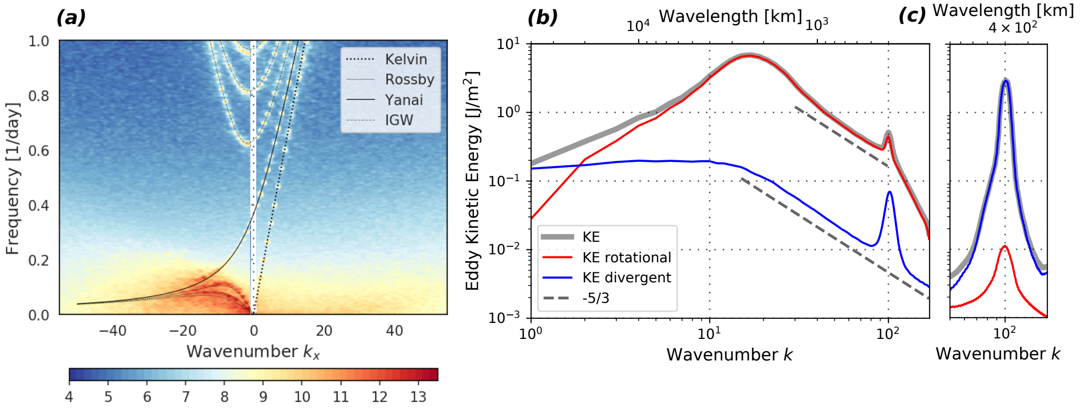

FIGURE 1 Tropical region spectra of dry vorticity-forced (a-b) and dry divergence-forced (c) runs: **(a)** Wavenumber-frequency diagram showing eddy potential energy (PE) from day 500 to 800 with a sampling frequency of 4 h^{-1} within an equatorial region between ±15° North/South (to retrieve the physical units J/m^2 from the colored contours the values have to be divided by their sampling size 10^8). Solid lines follow the theoretical dispersion relations of Kelvin, Rossby, Yanai, and Inertia Gravity waves. **(b)** Spatial spectra of total *(thick gray)*, vortical *(red)*, and divergent *(blue)* eddy KE. Two lines with $-5/3$ slopes are drawn for reference. **(c)** as in (b) but for the divergence-forced run (note that only a range near the forcing scale is shown). The spectra are based on the flow between ±20° North/South, averaged from day 200–1000 with daily sampling.

inverse transfer of KE (Salmon, 1998; Remmel and Smith, 2009), as has been confirmed in numerical simulations (Farge and Sadourny, 1989; Yuan and Hamilton, 1994). As seen in Figure 1b, in the equatorial region, the continuous forcing of vorticity with white noise in time at small scales also initiates an upscale transfer of energy that persists till the equatorial deformation scale ($\sqrt{c/\beta}$; approximately wavenumber 20 or 3500 km, where c represents the shallow-water wave speed). We emphasize that this represents the distribution of energy among different scales in the tropics as we have set the velocity field to zero outside ±20° before computing the spectrum. Here, KE is primarily composed of vortical modes and follows a $-5/3$ slope. The total eddy KE is a direct sum of the vortical and divergent eddy components (Appendix A). In fact, fundamentally, a general examination of adjustment of unbalanced initial conditions in the tropics suggests a split between balanced slow modes and fast inertia-gravity waves (Le Sommer et al., 2004). Thus, for tropical rotational modes, the appropriate suite of interactions, say for example on an equatorial β-plane, consists of Rossby triads (Ripa, 1983), and these appear to result in the inverse transfer seen in Figure 1b (see Appendix B for an explicit demonstration of the inverse KE flux). In particular, much like incompressible two-dimensional turbulence (Kraichnan, 1967), under small-scale forcing this $-5/3$ scaling represents an inverse energy transfer regime of geostrophic turbulence (Charney, 1971). We note that similarly forced quasi-linear versions of this run did not lead to an efficient transfer of energy to larger scales, instead they led to an accumulation of vortical eddy kinetic energy at the forcing scale (Table 1). On the other hand, a similar run but with no rotation ($f = 0$) showed a very efficient upscale cascade which halts at larger scales, affected by the frictional time scale (c.f. Appendix B, Figure 11). This supports the conclusion that the $-5/3$ scaling is a result of non-linear eddy-eddy interactions, and that its halting is due to Coriolis acceleration. Interestingly, though the divergent component has a comparatively much smaller amount of energy up to the deformation scale, we observe that it too scales with a $-5/3$ exponent and shows a pile up of energy at the forcing scale. The energy in these two components is consistent with estimates of the ratio of divergent to rotational energy in equatorial Rossby waves (Delayen and Yano, 2009).

As mentioned, the self-similar scaling of KE persists from the forcing scale to the deformation scale (approximately 3500 km). At even larger scales, energy projects on to the family of equatorial waves, possibly via a process analogous to the formation of

Rossby waves and jets in β−plane quasi-geostrophic turbulence (Rhines, 1977; Smith et al., 2002; Okuno and Masuda, 2003; Smith, 2004; Danilov and Gurarie, 2004; Suhas and Sukhatme, 2015). At these small wavenumbers, vortical eddy kinetic energy begins to decrease, the divergent modes gain strength and this coincides with the wave number range where equatorial waves were identified. Overall, the vortical energy dominates over the divergent contribution in the tropics (Yano et al., 2009), but at planetary scales, we find that the excited divergent modes are energetically comparable to the vortical modes. This is in line with the notion that particular classes of waves in the tropical atmosphere have a prominent divergent contribution at large scales (Yasunaga and Mapes, 2012). A caveat to keep in mind is that these largest scales can be sensitive to the damping employed in the numerical simulation. Further, we do not observe the breaking of large-scale Kelvin waves, which would be anticipated in non-dissipative scenarios and can influence interscale energy transfer (Boyd, 1980; Ripa, 1982; Bouchut et al., 2005).

For comparison, the KE spectrum for the run with mesoscale divergence forcing is shown in Figure 1c. In contrast to vorticity forcing (Figure 1b), energy essentially remains trapped at the forcing scale, and though there is a widening of the spectrum to all scales, unlike in the vorticity-forced case (Figure 1b), the kinetic energy remains by far largest at the forcing scale, and remains largely confined to region near it. Moreover, the divergent component is much larger than the rotational one, suggesting an ineffective transfer from the directly forced divergent flow to rotational modes. We note that the construction of the forcing function is such that it is restricted in absolute wavenumber, but it does project weakly onto larger scales in k_x and k_y, individually. As a result, even with divergent forcing, the normal modes of the system are excited and we see a very weak signature of tropical waves (Table 1). Further, the global mean eddy PE and divergent KE are of equal magnitudes (Table 1), as would be expected from small-scale linear gravity waves. It is likely that some of this divergent energy is in Kelvin waves, and once again, these waves can break and transfer energy to smaller scales with consequences for the parameterization of energy dissipation in more comprehensive models (Bouchut et al., 2005). The response to height forcing in the dry system (Figure 2) is intermediate between vorticity and divergence forcing scenarios. Specifically, while we do observe the formation of large-scale equatorial waves (Figure 2a) and the forcing indirectly excites rotational modes that transfer energy upscale (Figure 2b), at the same time energy accumulates and shows a maximum at the forcing scale itself. This is consistent with the excitation of equatorial waves via temporally correlated stochastic forcing (with a correlation time scale of a few days) of layer depth in a dry shallow-water model (Garfinkel et al., 2021). Interestingly, upscale transfer in the rotational component in this height forcing experiment is mediated by the ambient planetary vorticity (Figure 2c; KE flux is shown in Appendix B). Comparing Figures 2b and c, as anticipated from Equation 1 with $f = 0$, divergence (generated directly from h) is not able to excite vorticity and energy remains mainly contained in the divergent component itself. This is in contrast to the eddy-eddy rotational cascade in the vorticity forcing case which transports rotational KE upscale to values that exceed the forcing magnitude even in the absence of rotation (Appendix B).

The zonal mean eddy KE in the vortical and divergent modes as well as the zonal mean eddy potential energy (PE) as functions of latitude are shown in Figure 3. In all, the vortical energy is about two orders of magnitude larger than the divergent KE. Further, vortical KE attains a maximum in the equatorial region. Apart from being locally generated, this maximum could be due to an increasing Rossby radius of deformation towards the equator (Theiss, 2004), that allows for the inverse energy transfer to reach lower wave numbers that are capable of holding more energy (R. Salmon, personal communication). The magnitude of the eddy PE remains nearly constant outside the tropics but falls off almost monotonically from ±25° towards the equator. As the rotational zonal mean eddy KE increases towards the equator, the eddy PE decreases towards the equator and the conversion of eddy KE to eddy PE is less efficient in the tropical region. This is captured more clearly in Figure 3d which shows the ratio of eddy PE to rotational eddy KE. At higher latitudes this ratio nears unity but as we move into the tropics the value drops to a minimum of about 10^{-2} over the equator. Interestingly, the divergent kinetic energy is constant with latitude. Over time, the eddy KE composed of vortical and divergent modes reaches a quasi steady equilibrium in the fully turbulent flow. Compared to vortical eddy KE, eddy PE reaches equilibrium a bit later (as can be seen by comparing the convergence of curves in Figure 3a,c),

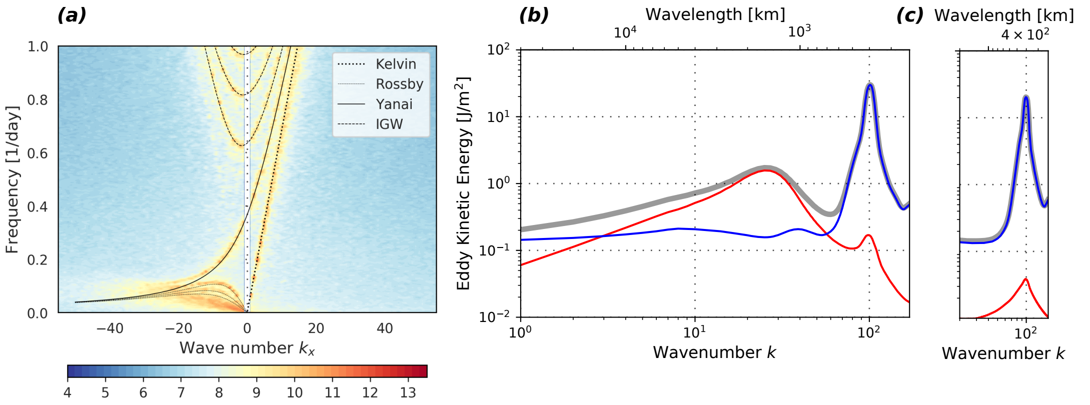

FIGURE 2 Tropical region spectra of the dry height-forced run. **(a)** Wavenumber-frequency diagram and dispersion curves. **(b)** Eddy KE spectra. **(c)** as in (b) but for a run with zero ambient planetary vorticity, i.e., $f = 0$. In **(b)** and **(c)**, the gray, red and blue lines show the KE of the total flow, of the vortical modes, and of the divergent modes, respectively.

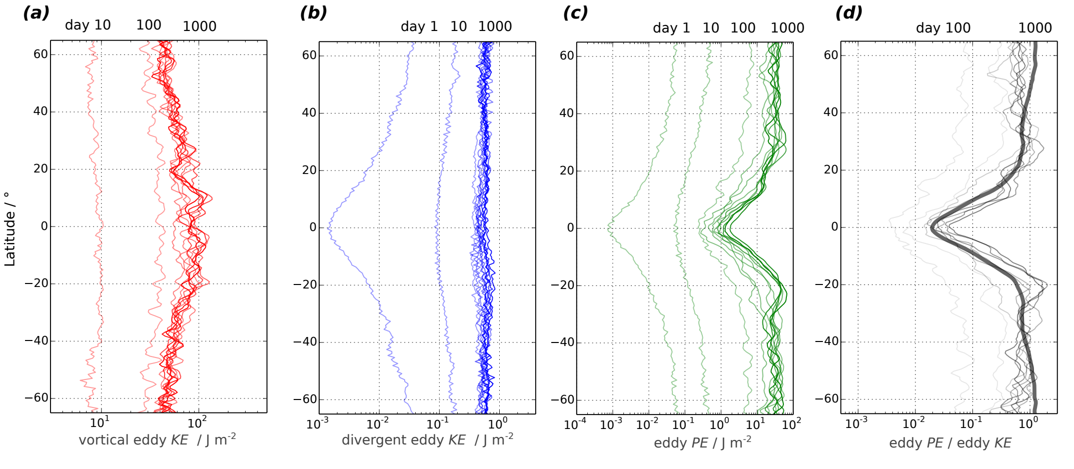

FIGURE 3 Zonally averaged latitudinal eddy energy profiles for different days along the integration for the dry vorticity-forced run (same run as in figure 1a,b) : **(a)** vortical eddy kinetic energy E_ψ, **(b)** divergent eddy kinetic energy E_ϕ, **(c)** eddy potential energy, **(d)** the ratio of eddy potential energy to eddy kinetic energy. In **(d)** the ensemble average on day 1000 over 80 runs is also shown as a thick gray line. The different curves from lighter (on the left) to darker (on the right) denote profiles on days $\in [1, 10, 100, 200, ..., 1000]$.

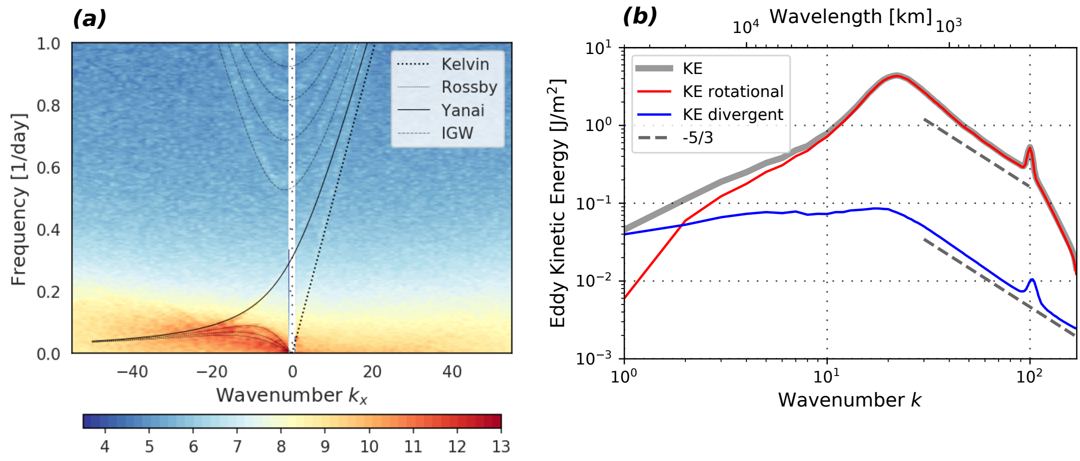

FIGURE 4 Tropical region spectra of the moist vorticity-forced run. **(a)** Wavenumber-frequency diagram and dispersion curves. **(b)** Eddy KE spectra with $-5/3$ lines for reference.

and at about half of the eddy KE magnitude.

4 | MOIST SIMULATIONS

Having established some properties of the dry system in the equatorial region, we now consider the moist shallow-water equations with small-scale vorticity forcing. We begin with the case when the background saturation field is uniform, i.e., q_s is a constant. The corresponding wavenumber-frequency diagram is shown in Figure 4a. Apart from a smooth background, we see signs of heightened activity along the westward propagating Rossby wave dispersion curves, the westward propagating part of the Yanai wave, and the lowest Kelvin wave modes with an appropriately reduced equivalent depth. In contrast to the dry simulation, where we saw a signature of all tropical waves (Figure 1a), the intensity of higher Kelvin waves, eastward propagating Yanai waves, and inertia-gravity waves can hardly be differentiated from the background spectrum. Again, small-scale forcing (around 400 km), as seen in Figure 4b, yields a $-5/3$ scaling with most of the energy in rotational modes. But, the inverse cascade is arrested at a smaller scale than in the dry case (Figure 1b). This is due to the fact that the equatorial deformation scale reduces in the presence of moisture by a factor of $\sqrt{(H - LQ)/H} = \sqrt{1 - LQ/H} \approx 0.7$ (where $Q = \max(q_s)$), shifting the maximum of the vortical KE spectrum from wavenumber 20 of the dry case to about wavenumber 28. Once again, in the mesoscale and synoptic scales, there are signs of similar scaling in the divergent modes, albeit with a much smaller amount of energy. At the largest scales, i.e., below wavenumber 10, the vortical mode energy falls off while the divergent KE remains relatively constant. The energy of vortical and divergent KE is again of comparable magnitude over the planetary range up to wavenumber 10 — like in spectra of the small-scale dry vorticity-forced experiment (Figure 1b). As in the dry case, eddy energy in the quasi-linear vorticity-forced run remains trapped at the forcing scale (not shown) which further suggests that the upscale energy transfer is mediated by nonlinear eddy-eddy interactions.

In the moist vorticity-forced run, the vortical and divergent KE, as well as the eddy potential and moist energies as functions of latitude for different times are shown in Figure 5. As for the dry case (Figure 3), vortical KE dominates over the divergent

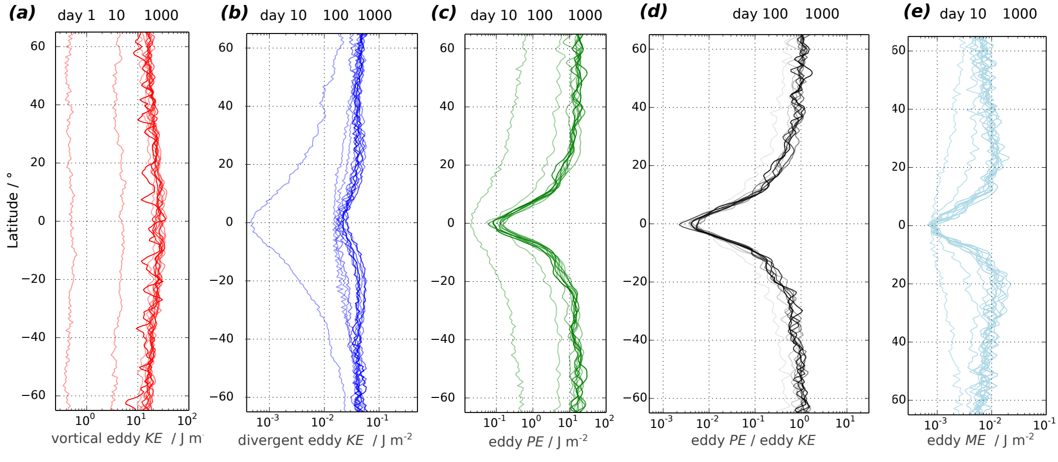

FIGURE 5 Similar diagnostics as Figure 3, but for the moist vorticity-forced run (shown in figure 4). In addition to dry diagnostics, eddy moist energy (ME) is plotted **(e)**.

part, and in fact, the difference between the two is much larger here (almost three orders of magnitude in the tropical region). Correspondingly, the ratio between global mean vortical and divergent eddy kinetic energy is larger than in the dry runs (Table 1). Rotational KE increases, again, monotonically towards the tropics while PE decreases monotonically towards the equator in the tropics. The latitudinal profile of the moist energy is similar to the one of the PE, but a few orders of magnitude weaker. The main difference is seen in the steady-state divergent KE, which decreases towards the equator in the moist run, while it is constant across the tropics in the dry run. We attribute this change to weaker equatorial Kelvin and inertia-gravity waves in the moist simulation (Figure 4a). Furthermore, the enhanced eddy ME may contribute most to an increase in divergent eddy KE in places in the sub-tropics, where it is maximum.

With stochastic small-scale divergent forcing, as in the dry case, energy remains in the divergent component and is trapped at the forcing scale with no signs of interscale energy transfer or a reddish background spectrum (figure not shown; Table 1). Forcing the height field in the moist situation produces large-scale equatorial waves (Figure 6a), even though it shows maximum energy at the forcing scale. Once again, experiments where the connection to divergence equation with planetary vorticity is broken by setting the Coriolis frequency f to zero, all energy remains at the forcing scale (Figure 6c). This indicates that the upscale transfer of eddy KE in moist stochastic height forcing is also mediated through the planetary vorticity (see Appendix B for the KE flux computation). In fact, an enhancement of upscale energy transfer in vortical modes at the mesoscale through planetary vorticity has been noted by Vallis et al. (1997). We further note the ratio of globally averaged eddy divergent KE and PE for the divergence forcing is again ≈ 1 (Table 1) — as in the dry divergence forced experiment. However, in this height-forced run, the ratio is 3. The larger ratio is again likely due to the projection and upscale transfer that we observe in the rotational modes. Finally, at the planetary scale, i.e., from wavenumbers 1–10, even though the rotational and divergent components behave similarly (comparing Figure 4a and Figure 6a), Kelvin, Yanai and inertia-gravity waves stand out in the moist height-forced experiments compared to the moist vorticity-forced runs, where Rossby waves dominate the wavenumber-frequency diagram.

In the moist scenario, an additional possibility that we explore is the effect of stochastically forcing the moisture field itself. As mentioned, our motivation for these experiments is to isolate the influence of random mesoscale moisture anomalies on the ensuing dynamics. As seen in Figure 7a, large-scale equatorial waves are produced with a magnitude comparable to height and

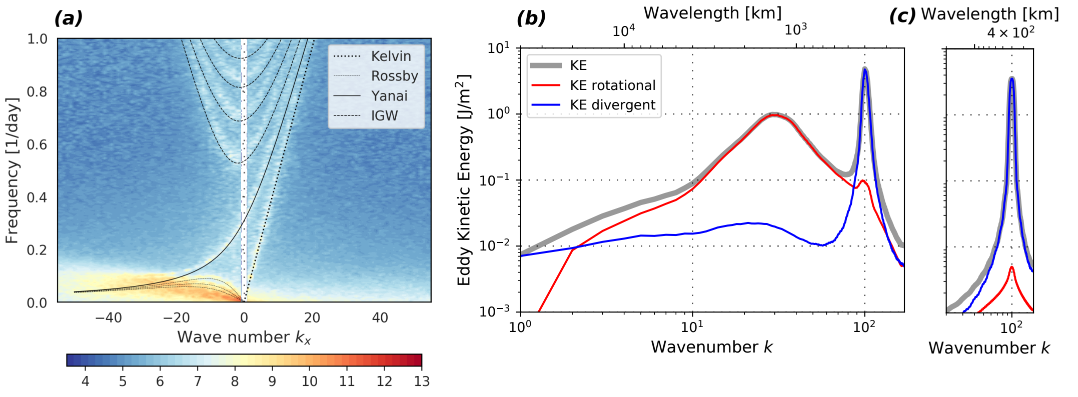

FIGURE 6 Same as figure 2, but for the moist height-forced runs.

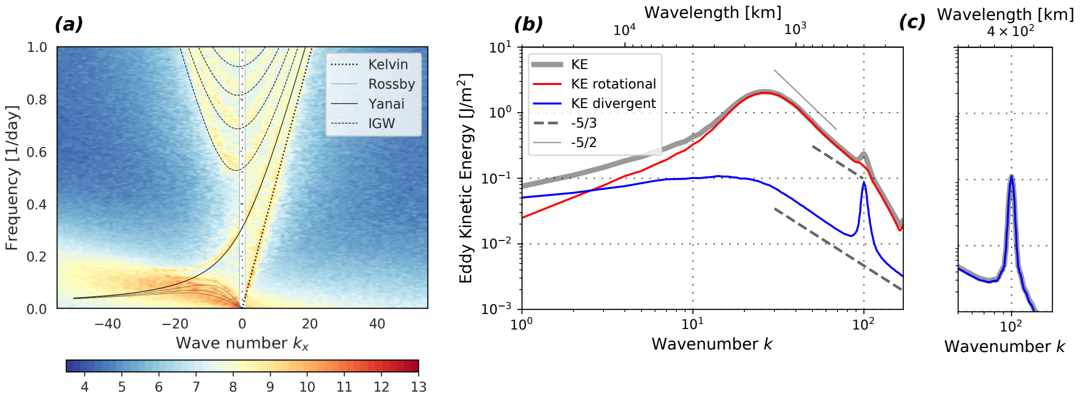

FIGURE 7 Same as figure 2, but for the moist moisture-forced runs. In **(b)**, the $-5/3$ slope *(black dashed)* and $-5/2$ slope *(gray line)* are added for reference.

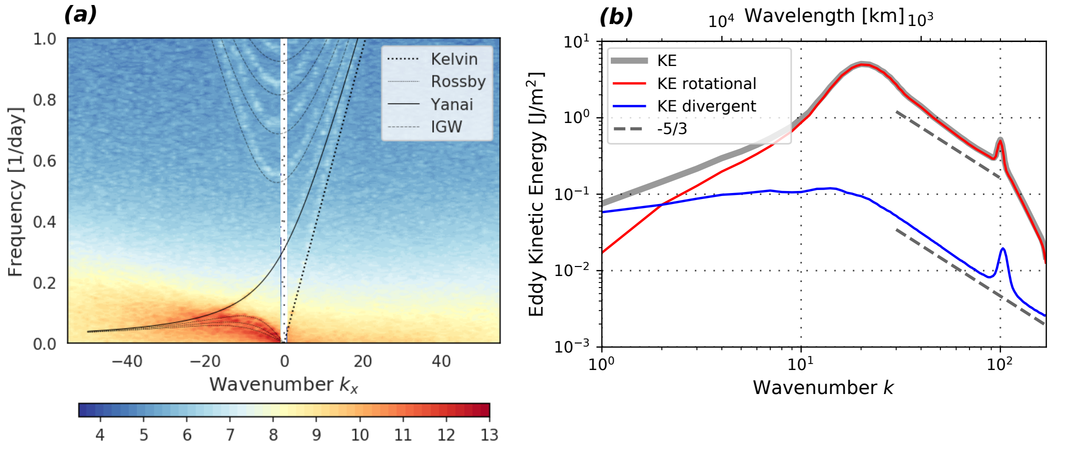

FIGURE 8 Same as figure 4 (moist vorticity-forced run), but with a stationary saturation background (q_s) depending on both latitude and longitude.

vorticity forcing. Further, once again, the entire family of tropical waves are discernible in the resultant wavenumber-frequency diagram. Moisture forcing also produces a robust inverse transfer among rotational modes (Figure 7b, Appendix B). In fact, even at the forcing scale, the rotational component is larger in magnitude than the divergent part, thus suggesting a more efficient transfer to rotational modes than in the height-forced scenario. There are signs of energy accumulating near the deformation scale and thus the KE spectrum is slightly steeper than the anticipated $-5/3$ exponent. As in the vorticity-forced experiments, the divergent component also scales with a power-law though it contains a smaller fraction of the total KE of the system. Finally, we note that, as in the inverse transfer with height forcing, the upscale flux is mediated by planetary rotation and if $f = 0$, then a clear local maximum of energy remains in the divergent component of the flow at the forcing scale (Figure 7c), while the vortical component in this case is negligible.

4.1 | Non-uniform background saturation

Precipitation in the tropics, at a given location, is observed to be tied quite closely to the amount of column water vapor present (Muller et al., 2009). Thus, given our formulation of condensation, it is natural to model the saturation field (q_s) as per column water vapor in the tropics. Keeping the actual distribution of precipitable water in the tropics in mind (Sukhatme, 2012), we consider two sets of non-uniform saturation fields. The first captures the latitudinal variation in precipitable water (Sobel et al., 2001; Sukhatme, 2013; Monteiro and Sukhatme, 2016). The second takes into account both a latitudinal and longitudinal structure, and falls off in the form of a Gaussian function both meridionally and zonally from the crossing of the dateline and the equator (Suhas and Sukhatme, 2020). The introduction of a spatial dependence of q_s is important as it introduces the possibility of condensation by means of rotational advection (Monteiro and Sukhatme, 2016), whereas for a constant saturation field condensation is only possible by means of divergence. In fact, the influence of background moisture fields on tropical modes has been noted in shallow-water studies (Sobel et al., 2001; Sukhatme, 2013; Dias et al., 2013), reanalysis data based examination of the Madden Julian Oscillation (Jiang et al., 2018) as well the birth of monsoon depressions in idealized and comprehensive models (Adames and Ming, 2018; Diaz and Boos, 2019; Adames, 2021; Diaz and Boos, 2021), but effects on moist turbulence have, as far as we know, not yet been studied.

We begin with q_s being a function of only latitude, specifically, it has a peak at the equator and falls off as we progress poleward. The KE spectra and wavenumber-frequency plots with small scale vorticity forcing are almost identical to the constant q_s case (hence, not shown), specifically, energy is mostly in westward propagating low-frequency modes and KE spectra are dominated by rotational modes that scale with a $-5/3$ exponent. When q_s depends on both latitude and longitude[1], the wavenumber-frequency diagram and KE spectra for small-scale vorticity-forced runs are shown in Figure 8. As seen in Figure 8a, we again have low-frequency Rossby waves whose equivalent depth matches a rapid condensation estimate. Note that between wavenumber 10-20 there is also a signature of westward propagating mixed Rossby gravity waves. Compared to the case when the background saturation is constant (Figure 4a), the excited inertia gravity waves, as well as the Kelvin and Yanai waves are more energetic. The excited higher frequency waves > $0.5\,\mathrm{day}^{-1}$ are slightly faster than the linear dispersion relations for the maximum saturation value Q. A reason for that is the contribution of dry regions on the globe, leading to a faster wave propagation (Gill, 1982). As the saturation declines zonally, the waves experience less reduced depths > 50 m and thus move faster. Clearly, there is a transfer of energy towards large scales (Figure 8b) and this is arrested near the equatorial deformation radius (approximately wavenumber 30), comparable to the previous purely dry simulation. In contrast, there is less accumulation of divergent eddy KE at the forcing scale than in the purely dry case, but more than in the moist run with a constant saturation background, consistent with this case having a combination of moister and dryer regions. Apparently stronger vortical modes are excited near the equatorial Rossby radius of deformation. The maximum kinetic energy is arrested at slightly higher magnitudes and smaller wavenumbers than in the case with constant background stratification in the log–log plot. As with other cases, divergence forcing in non-uniform saturation backgrounds does not lead to interscale energy transfer (Table 1).

4.2 | Emergence of moist coherent structures

A remarkable feature of the moist runs with vorticity forcing is the aggregation of moist anomalies into synoptic scale coherent structures by the turbulent flow. In fact, in equilibrium, spectra of moisture variance or eddy moist energy, shown in Figure 9 (row 1), follow a power-law scaling with an approximate -2 exponent. Though, note that ME is small in comparison to PE and KE_ζ which are of similar magnitude (Table 1). More importantly, Figure 9 also shows the temporal evolution of the moist spectra from an initially localized form near the forcing scale to moisture variance being distributed across scales, indicating that an inverse transfer of moist eddy energy occurs or that coherent structures in the eddy kinetic energy induce fluctuations in the moisture field. Indeed, the growth of moist anomalies at larger scales is strongly linked to the growth of coherent structures in the wind field as can be seen in rows 4 and 5 of Figure 9. To investigate this in more detail, we compute the spectral-space flux (Watanabe and Gotoh, 2004; Lindborg and Mohanan, 2017),

$$\mathrm{Flux}(k) = \int_k^\infty \mathcal{R}\left\{-\widehat{\nabla\cdot(\mathbf{v}\,s)}\,\widehat{s^*}\right\}\, d\widetilde{k}$$

where scalar s can be moist enthalpy $m = h - Lq$, moisture scaled with latent heat release Lq or height h, $\mathcal{R}$ denotes the real part, $\widehat{(\cdot)}$ marks complex variables in Fourier space depending on wavenumber $\widetilde{k}$, s^* is the complex conjugate of the scalar field s, and the integration ranges from wavenumber k to the largest possible wavenumber in the system. Note that this spectral-space flux is essentially the interscale flux of the variance of s, which is positive when the variance flux is downscale, and negative when it is

[1]The background spectrum $q_s(lat, lon) = \exp\left(-\frac{lat^2}{(60°)^2} - \alpha_0\,\frac{(lon-180°)^2}{(120°)^2}\right)$, where lat and lon are latitude and longitude in degrees, respectively. The constant $\alpha_0 = 0$ for the latitudinally varying, or $\alpha_0 = 1$ for the latitudinally and longitudinally varying background stratification.

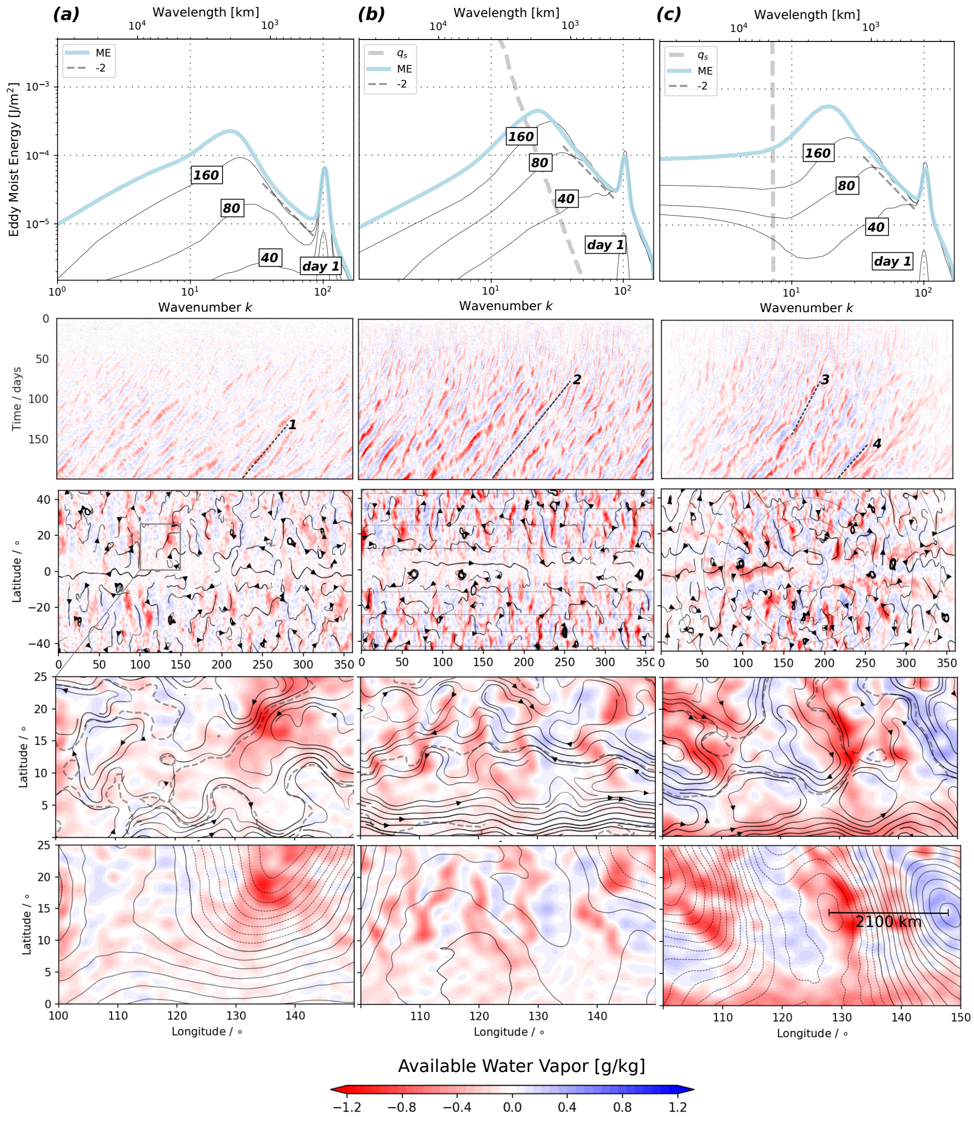

FIGURE 9 Characteristics of the moisture field, for the moist vorticity-forced runs, with three different moisture background fields - constant (left column), latitude-dependent (middle column) and latitude-longitude dependent (right column). **Row 1**: Spectra of eddy Moist Energy averaged over days 200-800 *(thick blue line)* alongside select days *(thin lines)* to show the time evolution. **Rows 2-5**: The distributions of available water vapor $q - q_s$ [g/kg] (in color) overlain on various other fields, as follows: **Row 2**: Longitude-time (Hovmöller diagram) at 20° North for days 0-200, with lines corresponding to propagation at different angular phase speeds *(dashed gray lines)* for four exemplary cases 1) -12.5°, 2) -7.5°, 3) -5.0°, and 4) -8.5° per 10 days. **Row 3**: Latitude-height distribution on day 900, with streamlines of vortical wind *(thin gray lines)*, and the background moisture distribution (thin gray lines) for the spatially varying q_s runs (middle and right columns). **Row 4**: A zoom-in of selected areas from Row 2 (marked by the rectangle in Row 3, right plot), with streamlines of the vortical wind, and an isoline of reduced depth of 50 m *(dashed gray line)*. **Row 5**: The same moisture field zomm-in of Row 4, but with positive/negative isolines *(solid/dashed black lines)* of the velocity potential Φ.

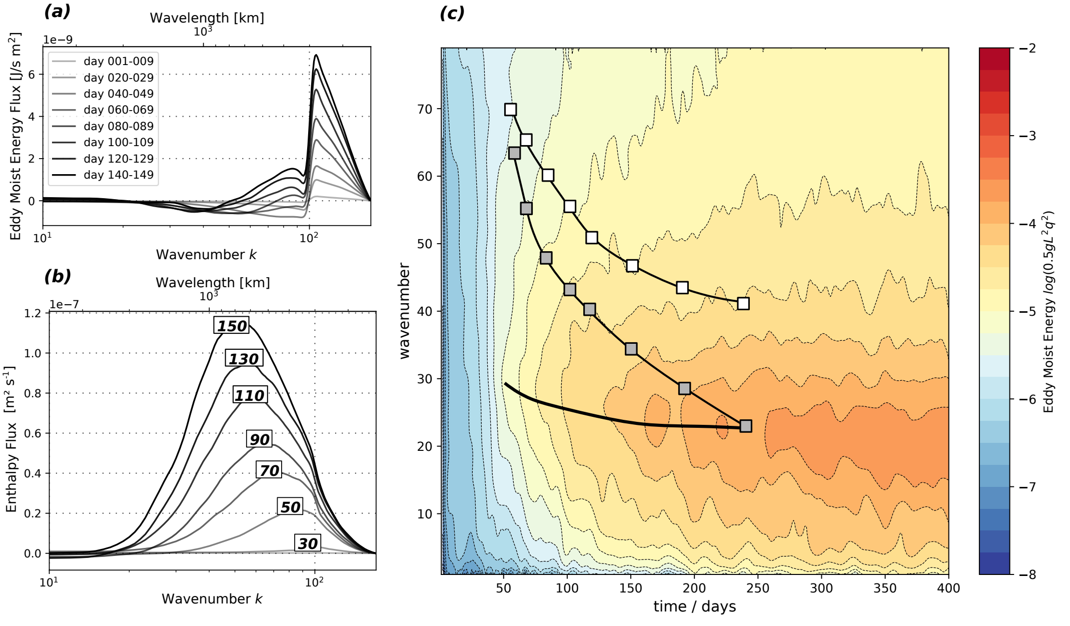

FIGURE 10 Moist energetics of the moist vorticity-forced run with a spatially constant background vorticity (same run as in Figure 4). **(a)** 10-day averages of the spectral-space eddy moist energy flux, from days 0-9 (lightest bottom line) to days 140-149 (dark upper-most line). **(b)** The temporal evolution of the spectral-space moist enthalpy flux for 10-day averages centered around the days noted in the boxes of each line. **(c)** Time-wavenumber plot of the moist energy (color shading, note this is the same quantity shown in figure 9a). Also shown for reference is the temporal evolution of the wavenumber of the maximum in moist energy *(thick solid black line)*, the wavenumber where upscale moist energy flux is strongest (the wavenumber of the minima of plot **(a)**) *(gray squares)*, and the wavenumber of maximum moist enthalpy flux shown in plot **(b)** *(white squares)*.

upscale. We note that the above term is obtained by adding the divergent flux$-\delta s s^*$ which is much smaller compared to the flux due to vortical advection (not shown), corresponding to much weaker divergent KE compared to rotational KE (Figure 8).

Specifically, we are interested in the eddy moisture flux. Noting that equation 1 gives us the time evolution of q' (since q_s is constant in time), multiplying it by q'^*, we get the equation for eddy ME. We note that the flux term has two contributions, a linear advection of the background q_s by the eddy field $\nabla \cdot (\mathbf{v} q_s) q'^*$, and a nonlinear term $\nabla \cdot (\mathbf{v} q') q'^*$, which we refer to as the eddy ME flux. For the constant q_s runs, the mean flow term is simply the divergence times q'^*. We find that this term is much smaller than the eddy ME flux (not shown).

The ME flux for the moist vorticity-forced run for a constant q_s is shown in Figure 10a. We see that it is negative for the first 150 days throughout the inertial range, and implies an upscale transfer of moisture variance. We also see that the eddy moist enthalpy flux is downscale (Figure 10b), and its maximum is a bit time delayed (Figure 10c) reaching smaller wavenumbers later than the peak of the upscale transfer of the ME flux. The moist eddy enthalpy transfer is mediated through a non-linear interaction of the evolving (vortical) wind $\mathbf{v}$ with moisture gradients ∇q from the small-scale stochastic forcing up through synoptic scales. The flux of ME is much smaller than that of KE flux, notably the evolving ME is also small compared to the evolving KE. As far as we are aware, such an emerging transfer of ME with a self-similar scaling of moist variance (Figure 9, top row) in a fully turbulent flow has not been explicitly demonstrated earlier. We also see that the inverse transfer of moisture variance differs from that of rotational KE. Specifically, at early times (i.e., before Day 50), the upscale moisture flux is observed from the forcing scale (400 km) to about 2000 km. Whereas, at later times (around Day 150), the inverse flux is only present at relatively larger synoptic scales, i.e., from about 900 km to 2000 km. In fact, at these later times, the moisture variance below 900 km is directed to small scales (Figure 10a).

For the spatially varying q_s runs, the spectral ME flux is dominated by the linear term, which is downgradient, essentially from the large scale of q_s, down to smaller scale. Interestingly, however, the eddy ME flux significantly increases compared to its value in the constant q_s runs, suggesting the existence of background moisture gradients not only modify the spectral characteristics of eddy ME by direct advection of moisture by the eddy flow field, but they also enhance the nonlinear cascades of eddy ME. Specifically we note that initial upscale cascade is five times larger in the spatially varying q_s runs compared to the constant background moisture runs. Indeed, it appears that, as suggested by Sobel (2002), water vapor can be viewed as a dynamically active scalar field and its cascade could be viewed in the context of the turbulence of such active scalar fields (Celani et al., 2004; Alexakis and Biferale, 2018). In addition to the weak upscale flux of moisture variance, somewhat similar to moist stratified 2D turbulence (Sukhatme et al., 2012), we observe that initially the moist energy grows almost exponentially across a range of wavenumbers (Figure 10c). Though, following this initial period, growth persists preferentially around the equatorial deformation scale which is where the equilibrium spectrum attains a maximum (first row of Figure 9 and the solid black line in Figure 10c).

The weak upscale transfer and growth of moist energy results in an aggregation of moist anomalies that is clearly visible in physical space Hovmöller diagrams shown in Figure 9 (row 2). Of course, it should be kept in mind that the development of moist coherent structures may be sensitive to the form of the moisture coupling to dynamics, and schemes that are significantly different than a Betts-Miller formalism may show different behaviour. This process takes place as time progresses, after about Day 75 in the constant q_s case, and somewhat earlier in the variable q_s cases. The inverse transfer is accelerated and strengthened when the background saturation q_s varies in space by up to a factor 5 at early times (not shown). Once formed, the coherent synoptic structures systematically drift westward in the tropical region. These westward propagating systems travel about 12.5° for constant background saturation, over 7.5° with latitudinally varying background, to 5.0° as well as 8.5° for latitudinally and longitudinally varying background within 10 days. We also note that these disturbances tend to increase in speed over time, in the case where background saturation varies in both horizontal directions. As was indicated by the KE spectra, in all cases,

Forcing	moist	$k^{-5/3}$	$\frac{\langle KE_\zeta \rangle}{\langle KE_\delta \rangle}$	$\frac{\langle PE \rangle}{\langle KE_\delta \rangle}$	$\frac{\langle ME \rangle}{\langle KE_\delta \rangle}$	runs	k_ζ	waves
f_ζ □ ○ ⨁		×	100	80		160	20	1
f_δ			1/50	1		1	100	10^{-5}
f_h ○			1/10	1		1	26	1
f_ζ, quasi-linear			1000	30		2	100	0
f_ζ □ ○ ⨁	×	×	400	100	1/10	80	28	1
f_δ	×		1/30	1	1/20	1	100	10^{-5}
f_h ○	×		3	3	1/20	1	30	1
f_q ○	×	×	200	100	20	80	26	1
f_ζ, quasi-linear	×		1000	100	1/20	2	100	0
f_ζ, varying q_s	×	×	300	100	1/80	2	22	1
f_δ, varying q_s	×		1/20	1	1/100	2	100	10^{-5}

TABLE 1 Overview of ensemble runs to indicate which experiments produce a rotational $k^{-5/3}$ upscale cascade, their associated wavenumber of the global maximum k_ζ of the vortical eddy KE, and the strength of waves compared to those generated with vorticity forcing. Global mean (denoted by $\langle \cdot \rangle$) ratios of vortical eddy KE $\langle KE_\zeta \rangle$, eddy PE $\langle PE \rangle$, and eddy ME $\langle ME \rangle$ to divergent eddy KE $\langle KE_\delta \rangle$ were calculated form day 800–1000. Quasi-linear experiments were run applying linearized momentum equations with respect to zonal mean velocities in the advection. The square □ further indicates that one of these stochastically forced ensemble members ran for at least 10,000 days. Additionally, experiments were run on a non-rotating Earth for the forcing marked with ○, as well as with increasing forcing amplitudes when marked with ⨁.

eddies form as energy cascades upscale. To view this mechanistically, we show snapshots of the moisture field, plotted along with different parts of the flow field (rows 3,4 and 5 of Figure 9). An examination of the close ups in rows 4 and 5 of Figure 9 tells us that the anomalies are largest for the case when the saturation field is a function of latitude and longitude. Further, the scale of the eddies (about 2100 km; Figure 9, row 5) agrees with estimates of the moist deformation radius. We note a strong correlation between the dry anomaly and a local minimum of the velocity potential ϕ in Figure 9 (row 5), which indicates a region of strong divergence as $\delta = \Delta\phi$ and proportional to $-k^2\phi$ in wave number space. Accordingly, the eddy divergent energy in varying background saturation is relatively stronger than for constant q_s (Table 1). In fact, strong divergent/convergent regions also correspond to vortical wind confluence regions, as can be deduced from Figure 9 (row 4). These moist coherent structures align with regions of converging streamlines but are aided by rotational advective condensation in the cases when the saturation field depends on space. For example, if we examine the flow at about 130° longitude and 15° N, the equatorward rotational flow brings parcels from a higher latitude towards the equator, resulting in a negative advective anomaly (red) as q_s is higher near the equator. This anomaly enhances the convergence induced condensation/evaporation in this region as it lies between two rotational gyres. In general, from the moisture equation in (1), the evolution of anomalies ($q^+, q^- \ll q_s$) involves advection operating on q_s and divergence multiplying the saturation field. Thus, moisture anomalies are co-located with divergence and convergence in the constant q_s case, but are influenced by the vortical meridional velocity in the $q_s(lat)$ case as well as by zonal advection in the $q_s(lat, lon)$ case.

5 | DISCUSSION

A detailed numerical investigation has been performed using the spherical dry and moist shallow-water systems to simultaneously investigate equatorial turbulence and large-scale tropical waves. In both moist and dry runs, small scale vorticity forcing (at approximately 400 km) results in a rotational mode dominated inverse transfer regime that persists up to the respective deformation scale. This scaling of the rotational kinetic energy complements the classic picture of geostrophic turbulence (Charney, 1971) and is similar to the more complicated moist model runs presented by Vallis et al. (1997). The dominance of rotational kinetic energy suggests that the inverse transfer of energy to larger scales involves equatorial Rossby triads (Ripa, 1983). Moreover, even though the divergent component has more than one order of magnitude less energy than the rotational part at synoptic scales, it also scales with a power-law and a $-5/3$ exponent. Mechanism denial quasi-linear simulations do not show an upscale transfer of energy thus highlighting the dynamical importance of nonlinear eddy-eddy interactions in this process. Notably, the existence of an inverse transfer of energy in the vortical component crucially depends on the type of variable that is being forced. While uncorrelated divergent forcing leads to an accumulation of energy at the forcing scale, as mentioned, vorticity forcing leads to a non-linear transport of energy through the synoptic scales. It should be kept in mind that our forcing of the divergent field is at small scales and stochastic in nature, and steady forcing at a larger scale might have different implications (Sardeshmukh and Hoskins, 1988). On forcing the height field, which can be viewed as proxy for temperature anomalies in the tropics, we observe behaviour that is intermediate to the purely divergence and vorticity forcing cases. Specifically, in both moist and dry systems, the peak of the energy spectrum remains at the forcing scale, but transfer to vortical modes does take place and this energy is then pushed up to larger scales. Forcing of the moisture field was formulated to represent a very idealized view of moist anomalies in mesoscale convective systems, and also leads to an inverse transfer of rotational KE; in fact, the generation of rotational modes in this case is more efficient than with height forcing. Though, it is important to note that the height and moisture-forced upscale transfer is different from the vorticity-forced case in the sense that they both require the presence of ambient planetary vorticity. In both these cases, planetary vorticity allows for the generation of vorticity from the divergent component of the flow.

With vorticity forcing, at planetary scales, divergent modes have comparable energy to the rotational modes and wavenumber-dispersion diagrams show the footprint of tropical waves. While the entire family of waves is seen in the dry runs, only low frequency modes stand out from the background spectrum in the moist cases. Further, much like results with temporally correlated height forcing (Garfinkel et al., 2021), our uncorrelated height forcing runs also result in the formation of large scale equatorial waves. Thus, in general, whenever we observe an upscale transfer of energy, we also observe the formation of large-scale equatorial waves. Though, subtle differences are noted in which member of the tropical wave family is preferentially excited by a given forcing. In all, while previous studies have simulated the emergence of equatorial waves through random forcing in the tropics (Garfinkel et al., 2021), or non-linear convective feedback (Yang and Ingersoll, 2013), this work explicitly demonstrates the formation and co-existence of planetary scale equatorial waves with a fully developed turbulent flow at synoptic scales.

In the vorticity-forced moist cases, the upscale energy transfer of KE is accompanied by moisture aggregation. Specifically, with vorticity forcing, it takes about a 100 days for coherent moist structures to appear. An examination of the interscale moist energy flux and spectra, as well as the moist enthalpy flux reveals different growth regimes during the formation of these aggregates. Initially, over approximately the first 50 days, the growth rate of ME is nearly exponential across a range of wavenumbers – a feature that has been noted in moist stratified turbulence (Sukhatme et al., 2012); then ME accumulates preferentially at larger wave numbers near the equatorial deformation radius. These two stages lead to an equilibrium moist energy spectrum that follows a power-law and scales with an exponent of approximately -2. Once formed, the aggregates propagate westward in the tropics with speeds of the order of a few meters per second. Further, during this initial period the ME flux also shows an inverse transfer. We argue that while later stages of the moist dynamics are certainly influenced by processes like the forward transfer of moist enthalpy and other local transport processes, for example, wave-eddy interactions (Garfinkel et al., 2021), the initiation of the aggregation crucially depends on the nonlinear interaction of vortical wind with moisture gradients. Moreover, in the small-scale vorticity-forced runs, moisture anomalies are largest in the case when the background saturation field depends on both longitude and latitude. Here, these anomalies are supported by advection and convergence, and are situated between the rotational gyres that dominate the tropics. It is important to note that coherent moist anomalies appear without radiative feedbacks or surface fluxes that are sometimes deemed to be essential ingredients in aggregation (for example, Wing et al., 2017). Taken together, these experiments showcase the concurrence of large-scale equatorial waves and fully developed turbulence in the dynamically evolving tropical region. The experiments further highlight the interdependence of rotational and divergent portions of the flow in such scenarios with a dynamically interactive moisture field.

We have focused on small-scale forcing in a single-layer shallow-water system, and in future work it would be interesting to simulate energy transfer in a multi-layer model that can resolve baroclinic instability (Schröttle et al., 2021). Such simulations provide a canonical source for a forward enstrophy cascade. Of course, with large-scale forcing that projects on to divergent modes there are also possibilities of Kelvin wave breaking that might lead to a more complex energy transfer scenario (Bouchut et al., 2005). Not only would this allow us to probe possible transitions from a -3 to $-5/3$ scaling in KE, the presence of large-scale baroclinic waves could serve as another source for low-frequency equatorial waves (Wedi and Smolarkiewicz, 2010). Possibly interscale energy transfer would occur that is coupled throughout the layers and involves a barotropization of the flow (Salmon, 1998), as well as the interaction of vertically sheared layers (Vallis et al., 1997). Generally, in a multi-layer model, studying the vertical circulation in space-time spectra of equatorial waves as done for numerical weather prediction reanalysis data (George Kiladis, personal communication) could especially be of interest, when vertical transport of moisture is explicitly resolved in dynamically coupled layers.

ACKNOWLEDGEMENTS

This work was conducted in a joint research project between the Israeli Science Foundation (grant number 2713/17) and University Grants Commission, India (grant number F6-3/2018). J. Schröttle wants to thank Adam Sobel and Rick Salmon for insightful discussions in the spring of 2019, as well as for the questions of all participants of the Meeting 'Physics at the equator: from the lab to the stars' in Lyon in October 2019. We furthermore thank Roy Barkan and his oceanography group at Tel Aviv University for inspiring discussions on geostrophic turbulence, as well as sharing their insights and diagnostic tools. J. Schröttle thanks Yair Cohen for always being available to discuss results and for helping to put them into context. We thank the reviewers for their comments which helped in the presentation of our work.

APPENDIX A. PARTITION OF ENERGY INTO ROTATIONAL AND DIVERGENT MODES

The sum of vortical kinetic energy KE_ζ and divergent kinetic energy KE_δ gives the total kinetic energy KE in spectral space. This can be deduced from Helmholtz decomposition of the velocity field in two-dimensional Fourier space. To retrieve correct units, the kinetic energy is normalized by domain mean height $\overline{H}$ and unit density $\rho = 1$ kg/m^3,

$$\begin{aligned} KE/\rho\overline{H} &= \frac{1}{2}\left(u^2 + v^2\right) = \frac{1}{2}\left(\left(u_\zeta + u_\delta\right)^2 + \left(v_\zeta + v_\delta\right)^2\right) = \\ &= \frac{1}{2}\left(u_\zeta^2 + 2\,u_\zeta u_\delta + u_\delta^2 + v_\zeta^2 + 2\,v_\zeta v_\delta + v_\delta^2\right) = \\ &= \frac{1}{2}\left(u_\zeta^2 + v_\zeta^2\right) + \frac{1}{2}\left(u_\delta^2 + v_\delta^2\right) + u_\zeta u_\delta + v_\zeta v_\delta . \end{aligned}$$

Using a Helmholtz decomposition with streamfunction ψ for vortical modes and potential ϕ for divergent modes, this equation can be rewritten. Thereby, (u_ζ, v_ζ) are the vortical modes of the wind and (u_δ, v_δ) are its divergent modes,

$$KE/\rho\overline{H} = \frac{1}{2}\nabla\psi \cdot \nabla\psi + \frac{1}{2}\nabla\phi \cdot \nabla\phi - \partial_y\psi\,\partial_x\phi + \partial_x\psi\,\partial_y\phi .$$

In Fourier Space the terms encapsulating vortical modes and divergent modes sum to zero,

$$\widetilde{KE} = \frac{1}{2}\left(k_x^2 + k_y^2\right)\tilde{\psi}^2 + \frac{1}{2}\left(k_x^2 + k_y^2\right)\tilde{\phi}^2 \underbrace{-k_y k_x \tilde{\psi}\tilde{\phi} + k_x k_y \tilde{\psi}\tilde{\phi}}_{=0} = \widetilde{KE}_\zeta + \widetilde{KE}_\delta ,$$

where $\tilde{\psi}$ and $\tilde{\phi}$ are the amplitudes of streamfunction and velocity potential in Fourier Space. Similarly, $\widetilde{KE}$, $\widetilde{KE}_\zeta$, $\widetilde{KE}_\delta$ are the amplitudes of kinetic energy, vortical kinetic energy, and divergent kinetic energy. In consequence, the total kinetic energy is a direct sum of vortical and divergent eddy kinetic energy as diagnosed previously in the spectral decomposition.

APPENDIX B. INTERSCALE FLUX OF KINETIC ENERGY

To calculate the flux of kinetic energy, we use

$$\text{KE Flux}(k) = \int_k^\infty \mathcal{R}\left\{-\frac{1}{2}\left(\widehat{u^*}\,\widehat{\mathbf{v}\cdot\nabla u} + \widehat{v^*}\,\widehat{\mathbf{v}\cdot\nabla v}\right)\right\}\, d\tilde{k} .$$

The KE spectrum without planetary rotation and interscale flux for the dry vorticity forcing with and without ambient rotation (i.e., $f \neq 0$ and $f = 0$) are shown in Figure 11. As is evident, the KE spectrum follows a $-5/3$ power-law that is dominated by rotational modes, though once again, the divergent modes also show a similar scaling. Further, even without planetary rotation, mesoscale vorticity forcing of the spherical shallow-water equations results in an upscale transfer of rotational KE. As far as we are aware, such an upscale transfer with $f = 0$ has not been demonstrated previously in the shallow-water equations. This is contrast to small-scale height forcing where $f = 0$ resulted in a lack of inverse KE transfer. KE fluxes for experiments with height forcing (dry & moist) and moisture forcing are shown in Figure 12. As is evident, an inverse transfer of rotational KE is observed in each of these cases; moreover, while of a similar order of magnitude, the upscale flux is more pronounced with mesoscale moisture forcing.

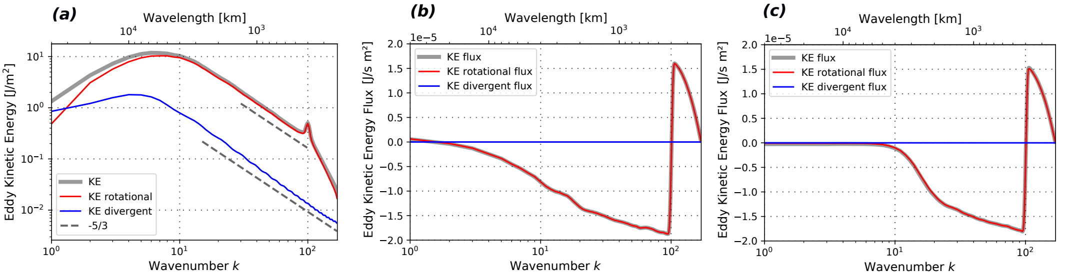

FIGURE 11 **(a)** Spatial KE spectra for the dry vorticity-forced run without Coriolis acceleration, for the total *(thick gray)*, vortical *(red)*, and divergent *(blue)* eddy KE. Also shown for reference are the $-5/3$ slopes (gray dashed lines). **(b)** The spectral-space flux of eddy KE for the run shown in **(a)**. **(c)** The spectral-space flux of eddy KE for the dry vorticity-forced run with Coriolis acceleration (run shown in figure 1b).

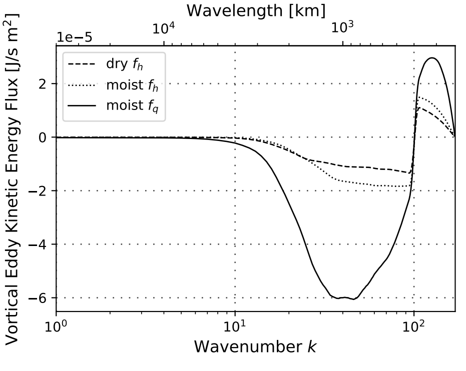

FIGURE 12 The spectral-space flux of eddy KE for the dry height-forced run (shown in figure 2), the moist height-forced run (shown in figure 6), and the moist moisture-forced run (shown in figure 7).

REFERENCES

ÁF Adames. Interactions between water vapor, potential vorticity, and vertical wind shear in quasi-geostrophic motions: Implications for rotational tropical motion systems. *Journal of the Atmospheric Sciences*, 78:903–923, 2021. doi: 10.1175/JAS-D-20-0205.1.

ÁF Adames and Y Ming. Interactions between water vapor and potential vorticity in synoptic-scale monsoonal disturbances: Moisture vortex instability. *Journal of the Atmospheric Sciences*, 75(6):2083–2106, 2018. doi: 10.1175/JAS-D-17-0310.1.

A Alexakis and L Biferale. Cascades and transitions in turbulent flows. *Physics Reports*, 767, 2018. doi: 10.1016/j.physrep.2018.08.001.

O Asselin, P Bartello, and D Straub. On boussinesq dynamics near the tropopause. *Journal of the Atmospheric Sciences*, 75:571–585, 2018. doi: 10.1175/JAS-D-17-0097.1.

P Bartello. Geostrophic adjustment and inverse cascades in rotating stratified turbulence. *Journal of the Atmospheric Sciences*, 52: 4410–4428, 1995. doi: 10.1175/1520-0469(1995)052<4410:GAAICI>2.0.CO;2.

E Bembenek, TM Merlis, and DN Straub. Influence of latitude and moisture effects on the barotropic instability of an idealized itcz. *Journal of the Atmospheric Sciences*, 78(9):2677—-2689, 2021. doi: 10.1175/JAS-D-20-0346.1.

L Bierdel et al. Accuracy of rotational and divergent kinetic energy spectra diagnosed from flight-track winds. *Journal of the Atmospheric Sciences*, 73:3273–3286, 2016. doi: 10.1175/JAS-D-16-0040.1.

GJ Boer and TG Shepherd. Large-scale two-dimensional turbulence in the atmosphere. *Journal of the Atmospheric Sciences*, 40: 164–184, 1983. doi: 10.1175/1520-0469(1983)040<0164:LSTDTI>2.0.CO;2.

F Bouchut, J Le Sommer, and V Zeitlin. Breaking of balanced and unbalanced equatorial waves. *Chaos: An Interdisciplinary Journal of Nonlinear Science*, 15(1):013503, 2005. doi: 10.1063/1.1857171.

F Bouchut, J Lambaerts, G Lapeyre, and V Zeitlin. Fronts and nonlinear waves in a simplified shallow-water model of the atmosphere with moisture and convection. *Physics of Fluids*, 21(11):116604, 2009. doi: 10.1063/1.3265970.

JP Boyd. The nonlinear equatorial kelvin wave. *Journal of Physical Oceanography*, 10(1):1–11, 1980. doi: 10.1175/1520-0485(1980)010<0001:TNEKW>2.0.CO;2.

J Callies, R Ferrari, and O Bühler. Transition from geostrophic turbulence to inertia–gravity waves in the atmospheric energy spectrum. *PNAS*, 111:17033–17038, 2014. doi: 10.1073/pnas.1410772111.

A Celani et al. Active and passive fields face to face. *New Journal of Physics*, 6, 2004. doi: 10.1088/1367-2630/6/1/072.

J Charney. Geostrophic turbulence. *Journal of the Atmospheric Sciences*, 28:1087–1095, 1971. doi: 10.1175/1520-0469(1971)028<1087:GT>2.0.CO;2.

P Chatterjee and BN Goswami. Structure, genesis and scale selection of the tropical quasi-biweekly mode. *Quarterly Journal of the Royal Meteorological Society*, 130:1171–1194, 2004. doi: 10.1256/qj.03.133.

JYN Cho and E Lindborg. Horizontal velocity structure functions in the upper troposphere and lower stratosphere: 1. observations. *Journal of Geophysical Research: Atmospheres*, 106(D10):10223–10232, 2001. doi: 10.1029/2000JD900814.

S Danilov and D Gurarie. Scaling, spectra and zonal jets in beta-plane turbulence. *Physics of Fluids*, 15, 2004. doi: 10.1063/1.1752928.

K Delayen and J-I Yano. Is asymptotic non-divergence of the large-scale tropical atmosphere consistent with equatorial wave theories? *Tellus*, 61:491–497, 2009. doi: 10.1111/j.1600-0870.2009.00404.x.

J Dias et al. Modulation of shallow-water equatorial waves due to a varying equivalent height background. *Journal of the Atmospheric Sciences*, 70(9):2726–2750, 2013. doi: 10.1175/JAS-D-13-04.1.

M Diaz and WR Boos. Monsoon depression amplification by moist barotropic instability in a vertically sheared environment. *Quarterly Journal of the Royal Meteorological Society*, pages 1–19, 2019. doi: 10.1002/qj.3585.

M Diaz and WR Boos. Monsoon depression amplification by moist barotropic instability in a vertically sheared environment. *Journal of the Atmospheric Sciences*, 78:1207–1225, 2021. doi: 10.1175/JAS-D-20-0286.1.

M Farge and R Sadourny. Wave-vortex dynamics in rotating shallow water. *Journal of Fluid Mechanics*, 206:433–462, 1989. doi: 10.1017/S0022112089002351.

DMW Frierson. Convectively coupled kelvin waves in an idealized moist general circulation model. *Journal of the Atmospheric Sciences*, 64(6):2076–2090, 2007. doi: 10.1175/JAS3945.1.

DMW Frierson, AJ Majda, and O Pauluis. Large scale dynamics of precipitation fronts in the tropical atmosphere: A novel relaxation limit. *Communications in Mathematical Sciences*, 2(4):591–626, 2004.

U Frisch and P-L Sulem. Numerical simulation of the inverse cascade in two-dimensional turbulence. *The Physics of fluids*, 27(8): 1921–1923, 1984. doi: 10.1063/1.864870.

CI Garfinkel, O Shamir, I Fouxon, and N Paldor. Tropical background and wave spectra: Contribution of wave–wave interactions in a moderately nonlinear turbulent flow. *Journal of the Atmospheric Sciences*, 78:1773–1789, 2021. doi: 10.1175/JAS-D-20-0284.1.

AE Gill. Some simple solutions for heat-induced tropical circulation. *Quarterly Journal of the Royal Meteorological Society*, 106(449): 447–462, 1980.

AE Gill. Studies of moisture effects in simple atmospheric models: The stable case. *Geophysical & Astrophysical Fluid Dynamics*, 19 (1-2):119–152, 1982. doi: 10.1080/03091928208208950.

HH Hendon and MC Wheeler. Some space–time spectral analyses of tropical convection and planetary-scale waves. *Journal of the Atmospheric Sciences*, 65:2936–2948, 2008. doi: 10.1175/2008JAS2675.1.

X Jiang et al. A unified moisture mode framework for seasonality of the madden–julian oscillation. *Journal of Climate*, 31(11): 4215–4224, 2018. doi: 10.1175/JCLI-D-17-0671.1.

B Khouider and AJ Majda. Equatorial convectively coupled waves in a simple multicloud model. *Journal of the Atmospheric Sciences*, 65(11):3376–3397, 2008. doi: 10.1175/2008JAS2752.1.

GN Kiladis et al. Convectively coupled equatorial waves. *Reviews of Geophysics*, 47(2), 2009. doi: 10.1029/2008RG000266.

Y Kitamura and Y Masuda. The k_h^{-3} and $k_h^{-5/3}$ energy spectra in stratified turbulence. *Geophysical Research Letters*, 33:L05809, 2006. doi: 10.1029/2005GL024996.

JN Koshyk and K Hamilton. The horizontal kinetic energy spectrum and spectral budget simulated by a high-resolution troposphere–stratosphere–mesosphere GCM. *Journal of the Atmospheric Sciences*, 58(4):329–348, 2001. doi: 10.1175/1520-0469(2001)058<0329:THKESA>2.0.CO;2.

RH Kraichnan. Inertial ranges in two-dimensional turbulence. *Physics of Fluids*, 10(7):1417–1423, 1967. doi: 10.1063/1.1762301.

Z Kuang. A moisture-stratiform instability for convectively coupled waves. *Journal of the Atmospheric Sciences*, 65(3):834–854, 2008a. doi: 10.1175/2007JAS2444.1.

Z Kuang. Modeling the interaction between cumulus convection and linear gravity waves using a limited-domain cloud system-resolving model. *Journal of the Atmospheric Sciences*, 65:576–591, 2008b. doi: 10.1175/2007JAS2399.1.

J Le Sommer, GM Reznik, and V Zeitlin. Nonlinear geostrophic adjustment of long-wave disturbances in the shallow-water model on the equatorial beta-plane. *Journal of Fluid Mechanics*, 515:135–170, 2004. doi: 10.1017/S0022112004000229.

J-L Lin et al. Tropical intraseasonal variability in 14 ipcc ar4 climate models. part i: Convective signals. *Journal of Climate*, 19: 2665–2690, 2006. doi: 10.1175/JCLI3735.1.

J-L Lin et al. The impacts of convective parameterization and moisture triggering on agcm-simulated convectively coupled equatorial waves. *Journal of Climate*, 21:883–909, 2008. doi: 10.1175/2007JCLI1790.1.

E Lindborg. Horizontal wavenumber spectra of vertical vorticity and horizontal divergence in the upper troposphere and lower stratosphere. *Journal of the Atmospheric Sciences*, 64:1017–1025, 2007. doi: 10.1175/JAS3864.1.

E Lindborg. A helmholtz decomposition of structure functions and spectra calculated from aircraft data. *Journal of Fluid Mechanics*, R4:762, 2015. doi: 10.1017/jfm.2014.685.

E Lindborg and G Brethouwer. Stratified turbulence forced in rotational and divergent modes. *Journal of Fluid Mechanics*, 587:83–108, 2007. doi: 10.1017/S0022112007007082.

E Lindborg and JYN Cho. Horizontal velocity structure functions in the upper troposphere and lower stratosphere: 2. theoretical considerations. *Journal of Geophysical Research*, 106:10233–10241, 2001. doi: 10.1029/2000JD900815.

E Lindborg and AV Mohanan. A two-dimensional toy model for geophysical turbulence. *Physics of fluids*, 29(11):111114, 2017. doi: 10.1063/1.4985990.

AJ Majda and MG Shefter. Models for stratiform instability and convectively coupled waves. *Journal of the Atmospheric Sciences*, 58: 1567–1584, 2001. doi: 10.1175/1520-0469(2001)058<1567:MFSIAC>2.0.CO;2.

BE Mapes. Convective inhibition, subgrid-scale triggering energy, and stratiform instability in a toy tropical wave model. *Journal of the Atmospheric Sciences*, 57:1515–1535, 2000. doi: 10.1175/1520-0469(2000)057<1515:CISSTE>2.0.CO;2.

T Matsuno. Quasi-geostrophic motions in the equatorial area. *Journal of the Meteorological Society of Japan. Ser. II*, 44(1):25–43, 1966. doi: 10.2151/jmsj1965.44.1_25.

JC McWilliams. The emergence of isolated coherent vortices in turbulent flow. *Journal of Fluid Mechanics*, 146:21–43, 1984. doi: 10.1017/S0022112084001750.

JM Monteiro and J Sukhatme. Quasi-geostrophic dynamics in the presence of moisture gradients. *Quarterly Journal of the Royal Meteorological Society*, 142(694):187–195, 2016. doi: 10.1002/qj.2644.

CJ Muller et al. A model for the relationship between tropical precipitation and column water vapor. *Geophysical Research Letters*, 36 (16), 2009. doi: 10.1029/2009GL039667.

GD Nastrom and KS Gage. A climatology of atmospheric wavenumber spectra of wind and temperature observed by commercial aircraft. *Journal of the Atmospheric Sciences*, 42:950–960, 1985. doi: 10.1175/1520-0469(1985)042<0950:ACOAWS>2.0.CO;2.

A Okuno and A Masuda. Effect of horizontal divergence on the geostrophic turbulence on a beta-plane: Suppression of the rhines effect. *Physics of Fluids*, 15, 2003. doi: 10.1063/1.1524188.

T N Palmer. A nonlinear dynamical perspective on model error: A proposal for non-local stochastic-dynamic parametrization in weather and climate prediction models. *Quarterly Journal of the Royal Meteorological Society*, 127(572):279–304, 2001.

M Remmel and LM Smith. New intermediate models for rotating shallow water and an investigation of the preference for anticyclones. *Journal of Fluid Mechanics*, 635:321–359, 2009. doi: 10.1017/S0022112009007897.

PB Rhines. Waves and turbulence on a β-plane. *Journal of Fluid Mechanics*, 69:417–443, 1977.

P Ripa. Nonlinear wave–wave interactions in a one-layer reduced-gravity model on the equatorial β plane. *Journal of Physical Oceanography*, 12(1):97–111, 1982. doi: 10.1175/1520-0485(1982)012<0097:NWIIAO>2.0.CO;2.

P Ripa. Weak interactions of equatorial waves in a one-layer model. part i: General properties. *Journal of Physical Oceanography*, 13: 1208–1226, 1983. doi: 10.1175/1520-0485(1983)013<1208:WIOEWI>2.0.CO;2.

M Rostami and V Zeitlin. Influence of condensation and latent heat release upon barotropic and baroclinic instabilities of vortices in a rotating shallow water f-plane model. *Geophysical & Astrophysical Fluid Dynamics*, 111(1):1–31, 2017. doi: 10.1080/03091929.2016.1269897.

M Rostami and V Zeitlin. Eastward-moving convection-enhanced modons in shallow water in the equatorial tangent plane. *Physics of Fluids*, 31(2):021701, 2019a. doi: 10.1063/1.5080415.

M Rostami and V Zeitlin. Geostrophic adjustment on the equatorial beta-plane revisited. *Physics of Fluids*, 31(8):081702, 2019b. doi: 10.1063/1.5110441.

R Salmon. *Lectures on geophysical fluid dynamics*. Oxford University Press, 1998.

PD Sardeshmukh and BJ Hoskins. The generation of global rotational flow by steady idealized tropical divergence. *Journal of the Atmospheric Sciences*, 45(7):1228–1251, 1988. doi: 10.1175/1520-0469(1988)045<1228:TGOGRF>2.0.CO;2.

N Schaeffer. Efficient spherical harmonic transforms aimed at pseudospectral numerical simulations. *Geochemistry, Geophysics, Geosystems*, 14(3):751–758, 2013. doi: 10.1002/ggge.20071.

J Schröttle, M Weissmann, L Scheck, and A Hutt. Assimilating visible and infrared radiances in idealized simulations of deep convection. *Monthly Weather Review*, 148(11):4357–4375, 2020. doi: 10.1175/MWR-D-20-0002.1.

J Schröttle, Y Cohen, N Harnik, E Heifetz, DL Suhas, and J Sukhatme. Upscale energy cascades on an idealized 3-level shallow earth. In *34th Conference on Hurricanes and Tropical Meteorology*. AMS, 2021.

RK Scott and LM Polvani. Forced-dissipative shallow-water turbulence on the sphere and the atmospheric circulation of the giant planets. *Journal of the Atmospheric Sciences*, 64:3158–3176, 2007. doi: 10.1175/JAS4003.1.

RK Scott and Lorenzo M Polvani. Equatorial superrotation in shallow atmospheres. *Geophysical Research Letters*, 35(24), 2008. doi: 10.1029/2008GL036060.

J Simpson et al. Mesoscale interactions in tropical cyclone genesis. *Monthly Weather Review*, 125:2643–2661, 1997. doi: 10.1175/1520-0493(1997)125<2643:MIITCG>2.0.CO;2.

KS Smith. A local model for planetary atmospheres forced by small-scale convection. *Journal of the Atmospheric Sciences*, 61(12): 1420–1433, 2004. doi: 10.1175/1520-0469(2004)061<1420:ALMFPA>2.0.CO;2.

KS Smith et al. Turbulent diffusion in the geostrophic inverse cascade. *Journal of Fluid Mechanics*, 469:13–48, 2002. doi: 10.1017/S0022112002001763.

A Sobel. Water vapor as an active scalar in tropical atmospheric dynamics. *Chaos: An Interdisciplinary Journal of Nonlinear Science*, 12(2):451–459, 2002. doi: 10.1063/1.1480795.

AH Sobel, J Nilsson, and LM Polvani. The weak temperature gradient approximation and balanced tropical moisture waves. *Journal of the Atmospheric Sciences*, 58(23):3650–3665, 2001. doi: 10.1175/1520-0469(2001)058<3650:TWTGAA>2.0.CO;2.

A Solodoch, WR Boos, Z Kuang, and E Tziperman. Excitation of intraseasonal variability in the equatorial atmosphere by Yanai wave groups via WISHE-induced convection. *Journal of the Atmospheric Sciences*, 68(2):210–225, 2011. doi: 10.1175/2010JAS3564.1.

DL Suhas and J Sukhatme. Low frequency modulation of jets in quasigeostrophic turbulence. *Physics of Fluids*, 27(1):016601, 2015. doi: 10.1063/1.4905710.

DL Suhas and J Sukhatme. Moist shallow water response to tropical forcing: Initial value problems. *Quarterly Journal of the Royal Meteorological Society*, 2020. doi: 10.1002/qj.3867.

J Sukhatme. Longitudinal localization of tropical intraseasonal variability. *Quarterly Journal of the Royal Meteorological Society*, 139 (671):414–418, 2012. doi: 10.1002/qj.1984.

J Sukhatme. Low-frequency modes in an equatorial shallow-water model with moisture gradients. *Quarterly Journal of the Royal Meteorological Society*, 2013. doi: 10.1002/qj.2264.

J Sukhatme and LM Smith. Vortical and wave modes in 3d rotating stratified flows: Random large-scale forcing. *Geophysical and Astrophysical Fluid Dynamics*, 102:437–455, 2008. doi: 10.1080/03091920801915318.

J Sukhatme, AJ Majda, and LM Smith. Two-dimensional moist stratified turbulence and the emergence of vertically sheared horizontal flows. *Physics of Fluids*, 24(3):036602, 2012. doi: 10.1063/1.3694805.

YQ Sun, R Rotunno, and F Zhang. Contributions of moist convection and internal gravity waves to building the atmospheric -5/3 kinetic energy spectra. *Journal of the Atmospheric Sciences*, 74:185–201, 2017. doi: 10.1175/JAS-D-16-0097.1.

YN Takayabu. Large-scale cloud disturbances associated with equatorial waves. part i: Spectral features of the cloud disturbances. *Journal of the Meteorological Society of Japan*, 72:433–448, 1994. doi: 10.2151/jmsj1965.72.3_433.

J Theiss. Equatorward energy cascade, critical latitude, and the predominance of cyclonic vortices in geostrophic turbulence. *Journal of Physical Oceanography*, 34(7), 2004. doi: 10.1175/1520-0485(2004)034<1663:EECCLA>2.0.CO;2.

R Tulloch and KS Smith. A theory for the atmospheric energy spectrum: Depth-limited temperature anomalies at the tropopause. *PNAS*, 103:14690–14694, 2006. doi: 10.1073/pnas.0605494103.

A Vallgren, E Duesebio, and E Lindborg. Possible explanation of the atmospheric kinetic and potential energy spectra. *Physical Review Letters*, 107:268501, 2011. doi: 10.1103/PhysRevLett.107.268501.

GK Vallis. *Atmospheric and Oceanic Fluid Dynamics*. Cambridge University Press, 2017.

GK Vallis and ME Maltrud. Generation of mean flows and jets on a beta plane and over topography. *Journal of Physical Oceanography*, 23(7):1346–1362, 1993. doi: 10.1175/1520-0485(1993)023<1346:GOMFAJ>2.0.CO;2.

GK Vallis and J Penn. Convective organization and eastward propagating equatorial disturbances in a simple excitable system. *Quarterly Journal of the Royal Meteorological Society*, 146, 2020. doi: 10.1002/qj.3792.

GK Vallis, GJ Shutts, and MEB Gray. Balanced mesoscale motion and stratified turbulence forced by convection. *Quarterly Journal of the Royal Meteorological Society*, 123(542):1621–1652, 1997. doi: 10.1002/qj.49712354209.

PT Vonich and GJ Hakim. Hurricane kinetic energy spectra from in situ aircraft observations. *Journal of the Atmospheric Sciences*, 75: 2523–2532, 2018. doi: 10.1175/JAS-D-17-0270.1.

ML Waite and C Snyder. Mesoscale energy spectra of moist baroclinic waves. *Journal of the Atmospheric Sciences*, 70:1242–1256, 2013. doi: 10.1175/JAS-D-11-0347.1.

B Wang, F Liu, and G Chen. A trio-interaction theory for madden–julian oscillation. *Geoscience Letters*, 3(1):34, 2016. doi: 10.1186/s40562-016-0066-z.

Y Wang et al. Mesoscale horizontal kinetic energy spectra of a tropical cyclone. *Journal of the Atmospheric Sciences*, 75:3579–3596, 2018. doi: 10.1175/JAS-D-17-0391.1.

T Watanabe and T Gotoh. Statistics of a passive scalar in homogeneous turbulence. *New Journal of Physics*, 6(1):40, 2004. doi: 10.1088/1367-2630/6/1/040.

NP Wedi and PK Smolarkiewicz. A nonlinear perspective on the dynamics of the mjo: Idealized large-eddy simulations. *Journal of the Atmospheric Sciences*, 67(4), 2010. doi: 10.1175/2009JAS3160.1.

M Wheeler and GN Kiladis. Convectively coupled equatorial waves: Analysis of clouds and temperature in the wavenumber–frequency domain. *Journal of the Atmospheric Sciences*, 56(3):374–399, 1999. doi: 10.1175/1520-0469(1999)056<0374:CCEWAO>2.0.CO;2.

M Wheeler, GN Kiladis, and PJ Webster. Large-scale dynamical fields associated with convectively coupled equatorial waves. *Journal of the Atmospheric Sciences*, 57(5):613–640, 2000. doi: 10.1175/1520-0469(2000)057<0613:LSDFAW>2.0.CO;2.

AA Wing et al. Convective self-aggregation in numerical simulations: A review. *Surveys in Geophysics*, 2017. doi: 10.1007/s10712-017-9408-4.

D Yang and A Ingersoll. Triggered convection, gravity waves, and the mjo: A shallow-water model. *Journal of the Atmospheric Sciences*, 70(8):2476–2486, 2013. doi: 10.1175/JAS-D-12-0255.1.

J-I Yano, S Mullet, and M Bonazzola. Tropical large-scale circulations: asymptotically non-divergent? *Tellus*, 61:417–427, 2009. doi: 10.1111/j.1600-0870.2009.00397.x.

K Yasunaga and BE Mapes. Differences between more divergent and more rotational types of convectively coupled equatorial waves. part ii: Composite analysis based on space–time filtering. *Journal of the Atmospheric Sciences*, 69:17–34, 2012. doi: 10.1175/JAS-D-11-034.1.

L Yuan and K Hamilton. Equilibrium dynamics in a forced-dissipative f-plane shallow-water system. *Journal of Fluid Mechanics*, 280: 369–394, 1994. doi: 10.1017/S0022112094002971.

V Zeitlin. *Geophysical fluid dynamics: understanding (almost) everything with rotating shallow water models*. Oxford University Press, 2018.